

$^{17}\text{O} + ^{58}\text{Ni}$ scattering and reaction dynamics around the Coulomb barrier

E. Strano,^{1,2,*} D. Torresi,^{1,2,†} M. Mazzocco,^{1,2} N. Keeley,³ A. Boiano,⁴ C. Boiano,⁵ P. Di Meo,⁴ A. Guglielmetti,^{5,6} M. La Commara,^{4,7} P. Molini,^{1,2} C. Manea,² C. Parascandolo,⁴ D. Pierroutsakou,⁴ C. Signorini,^{1,2,8} F. Soramel,^{1,2} D. Filipescu,⁹ A. Gheorghe,⁹ T. Glodariu,⁹ J. Grebosz,¹⁰ S. Jeong,¹¹ Y. H. Kim,¹¹ J. A. Lay,^{1,2} H. Miyatake,¹¹ M. Nicoletto,² A. Pakou,¹² K. Rusek,¹³ O. Sgouros,¹² V. Soukeras,¹² L. Stroe,⁹ N. Toniolo,⁸ A. Vitturi,^{1,2} Y. Watanabe,¹¹ and K. Zerva¹²

¹*Dipartimento di Fisica e Astronomia, Università di Padova, Via Marzolo 8, I-35131 Padova, Italy*

²*INFN - Sezione di Padova, Via Marzolo 8, I-35131 Padova, Italy*

³*National Centre for Nuclear Research, ul. Andrzeja Soltana 7, 05-400, Otwock, Poland*

⁴*INFN - Sezione di Napoli, Via Cintia, I-80126 Napoli, Italy*

⁵*INFN - Sezione di Milano, Via Celoria 16, I-20133 Milano, Italy*

⁶*Dipartimento di Fisica, Università di Milano, Via Celoria 16, I-20123 Milano, Italy*

⁷*Dipartimento di Scienze Fisiche, Università di Napoli, Via Cintia, I-80126 Napoli, Italy*

⁸*INFN - LNL, Viale dell'Università 2, I-35020 Legnaro (PD), Italy*

⁹*NIPNE, Str. Reactorului 30, P.O. Box MG-6, Bucharest-Magurele, Romania*

¹⁰*IFJ PAN, ul. Radzikowskiego 152, 31-342 Kraków, Poland*

¹¹*KEK, 1-1 Oho, Tsukuba, Ibaraki 305-0801, Japan*

¹²*Physics Department and HINP, University of Ioannina, Ipiros Mpizani 455 00, Ioannina, Greece*

¹³*Heavy Ion Laboratory, University of Warsaw, ul. Pasteura 5a, 02-093 Warsaw, Poland*

(Received 20 June 2016; published 31 August 2016)

This work aims at investigating the projectile binding energy influence on the reaction dynamics, introducing new results and new data analysis methods in order to overcome some typically encountered problems, such as the identification of reaction products differing by few mass units and the discrimination of direct reaction processes. The $^{17}\text{O} + ^{58}\text{Ni}$ collision was studied at five near-barrier energies employing a compact experimental setup consisting of four double-sided silicon strip detectors (DSSSDs). Different reaction processes, namely the elastic and inelastic scattering and the $1n$ stripping, were discriminated by means of a detailed analysis of the experimental energy spectra based on Monte Carlo simulations. The elastic scattering angular distributions were investigated within the framework of the optical model using Woods-Saxon and double-folding potentials. The total reaction cross sections were extracted and the reduced cross sections compared with those obtained for ^{17}F ($S_p = 0.600$ MeV), the mirror nucleus of ^{17}O ($S_n = 4.143$ MeV), and for the tightly bound ^{16}O projectile. The $^{17}\text{O} + ^{58}\text{Ni}$ total reaction cross sections were larger than those for ^{16}O on the same target at the lowest energies studied, becoming identical, within errors, as the incident energy increased above the Coulomb barrier. This behavior was related to a strong contribution from the $1n$ -stripping channel at the lowest energies.

DOI: [10.1103/PhysRevC.94.024622](https://doi.org/10.1103/PhysRevC.94.024622)

I. INTRODUCTION

With the increasing availability of radioactive ion beam (RIB) facilities, a growing interest in the reaction dynamics of collisions involving weakly bound nuclei has arisen. Many light nuclei, both stable and radioactive, are weakly bound and, especially in the case of exotic nuclei, are often characterized by unusual matter distributions or peculiar structures such as cluster states and nuclear halos, unique features which may significantly alter the reaction dynamics, especially at energies around the Coulomb barrier [1,2].

Despite the efforts made so far, a complete understanding of the reaction dynamics in collisions involving weakly bound nuclei has not been achieved yet. An exhaustive study of these collisions requires the discrimination of all the processes involved in the reaction dynamics and, with present technology, several difficulties are encountered:

- (1) Poor statistics, since RIB intensities are still several orders of magnitude lower than their stable counterparts.
- (2) The need to identify all reaction products, which may differ by only a few mass units and, in the case of neutrons, the need for high efficiency detection systems with sufficient angular resolution.
- (3) The cross sections for key processes may be very small, requiring rather long acquisition times, or show complicated kinematics, which might require coincidence measurements of reaction products in order to disentangle the reaction mechanisms.

Nevertheless, important information on a colliding system can be extracted by analyzing the elastic scattering, which in the past decades was a powerful tool for studies in the fields of nuclear structure, nuclear reaction theory, and nuclear astrophysics. Recently, the elastic scattering regained importance since, in the case of weakly bound and exotic nuclei, precise measurements can be analyzed in the framework of the optical model potential (OMP), giving information on the geometrical properties of the collision participants which might be very

*emanuele.strano@unipd.it

†School of Physics, University of Birmingham, Birmingham, B15 2TT, UK.

useful to correlate the matter distribution of a weakly bound nucleus and its structure to the reaction dynamics. Moreover the energy dependence of the OMP can efficiently probe the dynamics of the colliding systems [3,4]. In addition, an OMP analysis also allows the extraction of the total reaction cross section, providing information on the overall reactivity of the system. Despite several experimental and theoretical works highlighting that the total reaction cross sections for reactions involving weakly bound nuclei may be enhanced with respect to collisions involving tightly bound nuclei [5–7], a systematic relation between the total reaction cross section and the binding energy of the participants, like that suggested for the fusion process [8], has not been achieved yet, and a complete understanding of the influence of the binding energy on the total reaction cross section is still far from being determined [9–11].

An investigation of dynamical and structure effects in collisions involving weakly bound or exotic nuclei can be achieved by comparing similar systems which differ in the binding energy of the colliding nuclei, an example being the case of collisions involving ^{17}F and ^{17}O projectiles impinging on a ^{58}Ni target. ^{17}F is a proton drip-line nucleus, which can be described as a $^{16}\text{O} + p$ structure [12] where the weakly bound ($S_p = 0.6$ MeV) valence proton is in a $d_{5/2}$ level. Its first excited state exhibits proton halo properties [13] ($E^* = 495.3$ keV, $J^\pi = 1/2^+$). Its mirror nucleus, ^{17}O , has a neutron separation energy of $S_n = 4.134$ MeV and can be classified in an intermediate range between well bound ($S \sim 8$ MeV) and weakly bound nuclei ($S \lesssim 2$ MeV). ^{17}O can be described as either a $^{16}\text{O} + n$ structure or a $^{13}\text{C} + \alpha$ cluster structure [14,15], which may introduce more complex structure effects. A comparison between the two systems, taking into account the different Coulomb barriers, may hence show possible effects related to the different binding energies, and a further comparison with the $^{16}\text{O} + ^{58}\text{Ni}$ system may evidence effects related to the influence of the $^{17}\text{F} \rightarrow ^{16}\text{O} + p$ breakup and $(^{17}\text{O}, ^{16}\text{O}) 1n$ stripping processes.

Analyzing the elastic scattering angular distributions, at near-barrier incident energies in the framework of the optical model, it is possible to reveal a particular behavior, as a function of energy of the surface strengths of the real and imaginary parts, known as threshold anomaly (TA) [16–18]. In the usual TA, as the incident energy decreases below the Coulomb barrier the surface strength of the OMP is characterized by a reduction of its imaginary part corresponding to a “bump” in the real part. The decrease in the imaginary part is due to the progressive closure of the reaction channels, and both real and imaginary parts are correlated by means of a dispersion relation [16,17]. When the collision involves a weakly bound or exotic nucleus, the OMP trend may show an unusual behavior, as the incident energy decreases below the Coulomb barrier, being characterized by an increase of the imaginary part [19–21]. Some authors named this behavior “breakup threshold anomaly” [22]. A comparison of the behavior of the OMP as a function of the incident energy for the $^{17}\text{O} + ^{58}\text{Ni}$ and $^{16}\text{O} + ^{58}\text{Ni}$ systems may reveal effects due to the $^{16}\text{O} + p$ structure of ^{17}O and the influence of the $(^{17}\text{O}, ^{16}\text{O}) 1n$ stripping reaction channel on the elastic scattering.

Summarizing, there are several motivations for studying the $^{17}\text{O} + ^{58}\text{Ni}$ elastic scattering. A comparison of new $^{17}\text{O} + ^{58}\text{Ni}$ data with those available for the $^{17}\text{F} + ^{58}\text{Ni}$ system could constitute a probe for testing effects related to the different binding energies of ^{17}F , ^{17}O , and ^{16}O , whereas a comparison with the $^{16}\text{O} + ^{58}\text{Ni}$ elastic scattering should underline possible effects connected to the $1n$ stripping. The experiment described in this work was intended as a doorway for studies involving radioactive ion beams, thus providing a test case for the development of analysis techniques which allow the discrimination of different processes occurring in the collision. In fact, the discrimination of the reaction products is not always possible, especially in the case where the products stop in the first detection stage of the telescope with an energy similar to the projectile one (and often the same charge, as in the cases of the $1n$ pickup and the $1n$ stripping).

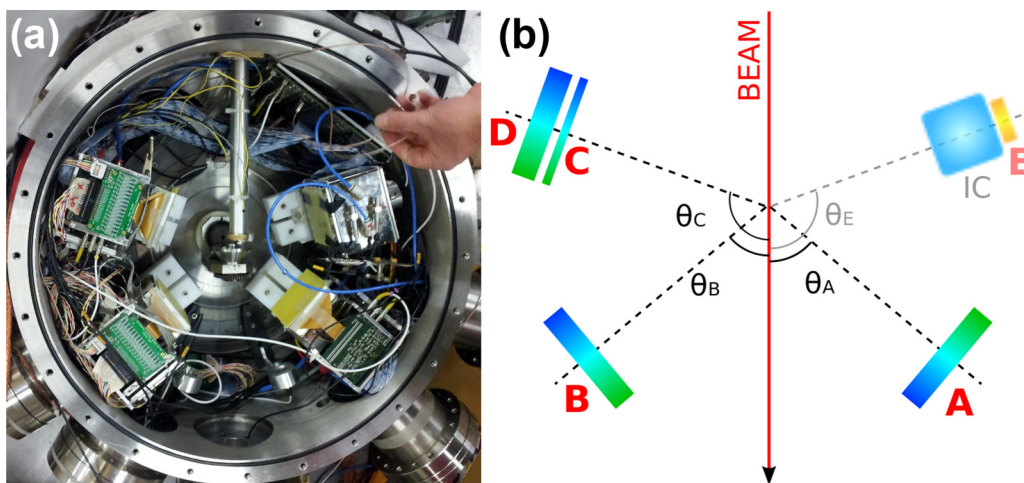


FIG. 1. (a) Photograph of the experimental setup. (b) Schematic view of the experimental setup. A, B, and D are $300 \mu\text{m}$ thick DSSSDs; C is a $43 \mu\text{m}$ thick DSSSD. An additional telescope IC/E consisting of an ionization chamber (IC) followed by a $100 \mu\text{m}$ thick surface barrier detector (E) was located at a backward angle.

The $^{17}\text{O} + ^{58}\text{Ni}$ collision was investigated employing the experimental setup described in Sec. II. The data analysis procedure for the discrimination of the processes and the extraction of the angular distributions is detailed in Sec. III. Section IV describes the optical model analysis of the elastic scattering angular distributions carried out employing three different approaches. The results are reviewed and discussed in Sec. V and some conclusions are made in Sec. VI.

II. EXPERIMENT

The experiment was performed at the Laboratori Nazionali di Legnaro (LNL), Italy, using a ^{17}O beam delivered by the Tandem XTU accelerator with an average current of about 15 nA. Beam energies were varied in steps of 2.5 MeV in the range 40.0–50.0 MeV. Beam particles impinged on a ^{58}Ni (99.48% enriched) $150 \mu\text{g}/\text{cm}^2$ thick target with a ^{208}Pb (99.57% enriched) $50 \mu\text{g}/\text{cm}^2$ thick backing. Three collimators of diameters $\phi_1 = 2$ mm, $\phi_2 = 1$ mm, and $\phi_3 = 3$ mm, respectively, were placed 250, 30, and 10 mm upstream of the target, defining a $\phi \simeq 1$ mm beam spot on the target. A photograph of the scattering chamber and a schematic view of the experimental setup are shown in Fig. 1. Four double-sided silicon strip detectors (DSSSDs) with an active area of $62.5 \text{ mm} \times 62.5 \text{ mm}$ were employed. Each DSSSD was segmented into 32 strips per side, defining pixels whose surface is $\sim 2 \times 2 \text{ mm}^2$. Three of the DSSSDs, labeled A, B, and D in Fig. 1, were $300 \mu\text{m}$ thick, whereas that labeled C was $43 \mu\text{m}$ thick. Detectors A and B were placed at forward angles symmetrically with respect to the beam axis: the center of DSSSD A (B) was placed at $\theta_{A(B)} = 49.4^\circ$ (-49.5°) at a distance of 119.9 mm (118.4 mm) from the target, covering the angular range $36^\circ < \theta_{\text{lab}} < 65^\circ$. The telescope consisting of detector C followed by detector D was placed in the backward hemisphere at $\theta_C = -110.8^\circ$ (telescope center) and a distance of 107.3 mm from the target, covering the angular range $94^\circ < \theta_{\text{lab}} < 125^\circ$. An additional telescope consisting of an ionization chamber (labeled IC in Fig. 1) followed by a $100 \mu\text{m}$ thick surface barrier detector (labeled E in Fig. 1) placed at $\theta_E = 108.2^\circ$ and a distance of 125.3 mm from the target was employed for testing the EXPADES [23,24] detector array components. The IC/ E_{res} telescope was commissioned in this run.

Detectors A and D were equipped with an application-specific integrated circuit (ASIC) based electronics chain developed for the E_{res} stage of the EXPADES array and allowing a full granularity of 32×32 pixels. Detectors B and C were connected to analog electronics chains developed for the ΔE stage of the EXPADES array. In order to contain the cost of the electronics, strips of detectors B and C were short-circuited two-by-two in the preamplification stage front end (16×16 granularity). Further details may be found in Refs. [23,24].

III. DATA ANALYSIS

A. Discrimination of processes

Figure 2 shows the energy spectra collected by the back side (vertical strips) of detector A at a beam energy of $E_{\text{lab}} =$

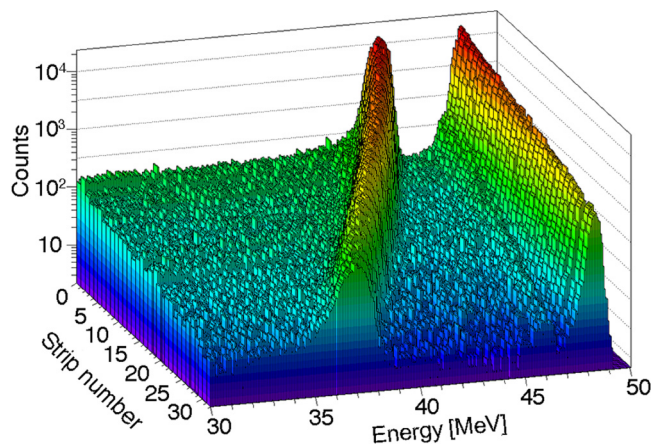


FIG. 2. Energy spectra collected by the back side (vertical strips) of detector A at a beam energy of $E_{\text{lab}} = 50$ MeV. In this three-dimensional plot the energy spectra of individual strips are plotted sequentially along the “strip number” axis from the most forward polar angle (strip 0) to the most backward polar angle (strip 31). The peak at higher (lower) energy corresponds to the ^{17}O scattering from the ^{208}Pb (^{58}Ni) target. The kinematics of the $^{17}\text{O} + ^{58}\text{Ni}$ collision is visible as the strip number (i.e., polar angle) increases.

50 MeV. The energy spectra of individual strips are plotted sequentially along the perspective axis labeled “strip number,” strip 0 (31) being located at the most forward (backward) polar angle. Since a composite target (^{58}Ni with a ^{208}Pb backing) was used, each energy spectrum is characterized by two peaks: the former located at higher energies, corresponding to the ^{17}O scattering from the ^{208}Pb target layer, the latter located at lower energies, corresponding to the ^{17}O interaction with the ^{58}Ni target layer. The energy separation between the two peaks increases as the strip number (i.e., scattering angle) increases due to linear momentum conservation. Calibration of energy spectra was performed by means of a standard ^{239}Pu , ^{241}Am , ^{244}Cm α source ($E_\alpha = 5.155$, 5.486 , and 5.805 MeV, respectively) and by using the centroid of the peak corresponding to the elastic scattering from the ^{208}Pb target layer as a fourth calibration point (employing Ziegler’s tables [25] for the evaluation of the energy losses in both target layers of the target before and after the collision). The overall FWHM energy resolution of a strip (electronic noise and detector intrinsic resolution) was found to be about 1–1.4% for an α -particle energy of 5.805 MeV.

Four phenomena can contribute to the peak originating from the $^{17}\text{O} + ^{58}\text{Ni}$ interaction: (a) the elastic scattering of ^{17}O ions from the ^{58}Ni target; (b) the one-neutron stripping reaction $^{17}\text{O} + ^{58}\text{Ni} \rightarrow ^{16}\text{O} + ^{59}\text{Ni}$, $Q_{\text{gg}} = 4.856$ MeV; (c) the inelastic scattering process leaving the ^{17}O projectile in its first excited state ($E^* = 871$ keV $J^\pi = 1/2^+$); and (d) the inelastic scattering process leaving the ^{58}Ni target in its first excited state ($E^* = 1.454$ MeV, $J^\pi = 2^+$). Explorative continuum discretized coupled channel (CDCC) calculations indicated that the projectile breakup $^{17}\text{O} \rightarrow ^{16}\text{O} + n$ should provide a

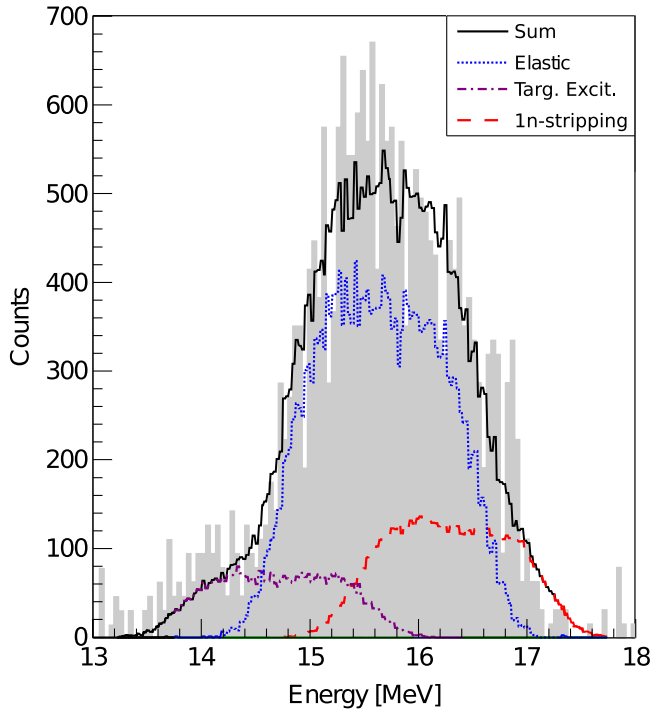


FIG. 3. Detail of the energy spectrum collected by a vertical strip at $\theta_{\text{lab}} = 119^\circ$ and $E_{\text{lab}} = 42.5$ MeV and related to the $^{17}\text{O} + ^{58}\text{Ni}$ interaction. The experimental distribution (gray filled) shows binning-independent structures which indicate the contribution of more than one process. An example of the fitting procedure used for the discrimination of processes is also shown. The solid (black) line corresponds to the fitting function [Eq. (3.1)] which is the sum of four processes. The dotted line (blue), the dash-dotted line (purple), and the dashed line (red) represent the elastic scattering, the target excitation and the $1n$ stripping renormalized MC-simulated distributions, respectively. The contribution of the projectile excitation was found to be negligible at all energies.

negligible contribution, especially considering the 4.13 MeV binding energy of the valence neutron.

At forward angles the fractions of processes **b**, **c**, and **d** were observed to be negligible with respect to the integral of the elastic peak, whereas at backward angles all the processes must be properly taken into account. ^{17}O (^{16}O) ions leaving the target at backward angles were completely stopped in the ΔE stage (detector C) of the silicon telescope, therefore the algorithm for the discrimination of the processes was employed only for events detected by detector C. Several Monte Carlo (MC) simulations were performed in order to reproduce accurately the observed spectra. In these MC simulations the following conditions and calculations were considered:

- (1) A two-dimensional (2D) Gaussian distribution (with $\sigma = 0.5$ mm) for the impact coordinates on the target plane, according to the beam spot size defined by the collimation system on the target surface.
- (2) A uniform distribution for the depth of impact inside the target (responsible for $\sim 95\%$ of the peak width).

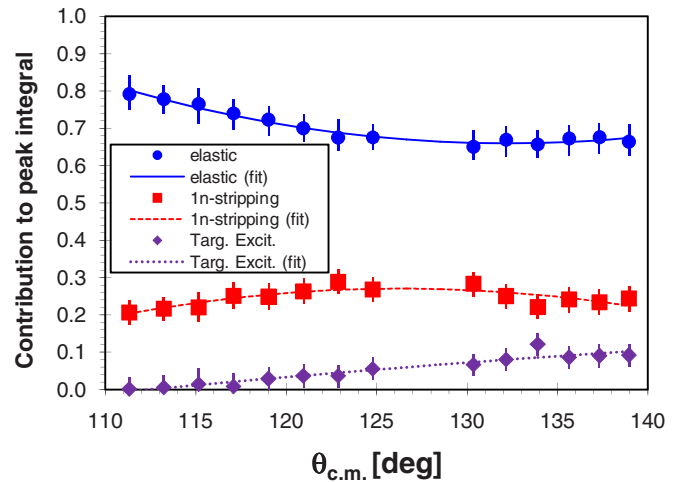


FIG. 4. Fractions of the contribution from elastic scattering (process **a**, blue circles), $1n$ stripping (process **b**, red squares), and target excitation (process **d**, purple diamonds) to the peak corresponding to the $^{17}\text{O} + ^{58}\text{Ni}$ collision at $E_{\text{lab}} = 42.5$ MeV for the backward detector C. The contribution of the projectile excitation was negligible. Each contribution was fitted with a second-order polynomial (solid, dashed, and dotted lines for the elastic scattering, $1n$ stripping, and target excitation, respectively).

- (3) The energy loss and energy straggling in the target before the collision, calculated employing Ziegler's tables [25].
- (4) The elastic scattering process was simulated according to the Rutherford differential cross section in order to reproduce the kinematic broadening along each strip.
- (5) The kinematics of the one-neutron stripping process was simulated according to the semiclassical model of Brink [26].
- (6) The energy loss and energy spread in the remaining target portion.
- (7) An exponential distribution for a phenomenological description of the processes (e.g., multiple scattering [27]) responsible for the exponential tails in the low-energy side of both experimental peaks.
- (8) The energy loss and energy spread in the detectors dead layer.
- (9) A target nonuniformity of 15% FWHM [28] as found from the study of the $^{17}\text{O} + ^{208}\text{Pb}$ elastic scattering and the electronic noise of the system (see details in Ref. [24]).

In the first step of the data analysis the energy spectra collected by the vertical strips were examined. Events not detected within the full energy peaks of both vertical and horizontal strips (i.e., interstrip events on either detector side) were rejected and the background was removed. The spectra of the ^{17}O elastic scattering from the ^{208}Pb backing layer were adequately reproduced by the MC simulations using the terms contributing to the $^{17}\text{O} + ^{208}\text{Pb}$ elastic scattering peak width. The low-energy tail of the $^{17}\text{O} + ^{208}\text{Pb}$ elastic peak was fitted with an exponential function. The parameters of the exponential fit, which are functions of both the detection

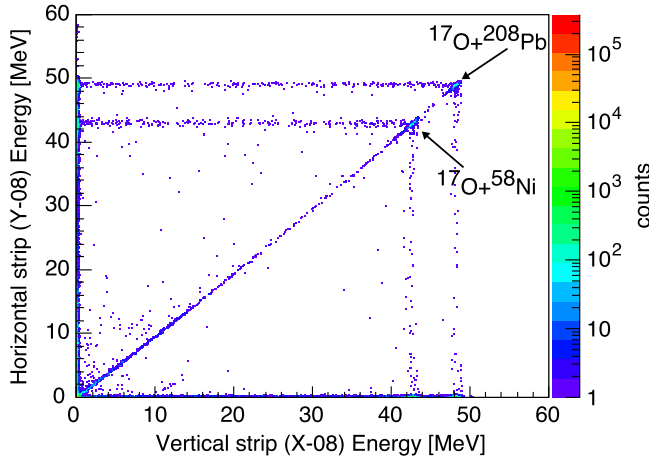


FIG. 5. Pixel correlation plot of vertical strip number 8 versus horizontal strip number 8 for detector A at $E_{\text{lab}} = 50$ MeV. The two spots (indicated by the arrows) at ~ 43 MeV and ~ 48 MeV correspond to the full energy peaks of ^{17}O particles scattered from the ^{208}Pb backing and ^{17}O (^{16}O) originating from the interaction with the ^{58}Ni target. Events distributed along the horizontal and vertical lines (at strip energies of ~ 43 and ~ 48 MeV) correspond to interstrip events on either side of the detector.

angle and the bombarding energy, were introduced into the simulations as a probability distribution which was applied to the detected energy of each event.

The processes **a**, **b**, **c**, and **d** were individually simulated for each investigated beam energy. The simulated energy spectra in the laboratory frame were generated for each vertical strip of detector C and then normalized to their respective integrals. These “normalized” spectra were used as numerical functions (f_a , f_b , f_c , and f_d for the processes **a**, **b**, **c**, and **d**, respectively) for a χ^2 minimization best-fit of the peak related to the $^{17}\text{O} + ^{58}\text{Ni}$ interaction in the experimental spectra. In particular, the following parametric numerical function was employed:

$$f_{\text{exp}}(E, \theta) = Af_a(E, \theta) + Bf_b(E, \theta) + Cf_c(E, \theta) + Df_d(E, \theta), \quad (3.1)$$

where A , B , C , and D are the best-fit parameters corresponding to the contributions of processes **a**, **b**, **c**, and **d**, respectively. Figure 3 shows a zoom of the energy spectrum collected for $\theta_{\text{lab}} = 119^\circ$ and $E_{\text{lab}} = 42.5$ MeV in the region where the peak corresponding to the $^{16}\text{O} + ^{59}\text{Ni}$ interaction is located. The observed structures, which indicate the presence of several contributing processes, were well reproduced by the fitting function of Eq. (3.1).

The best-fit parameters A , B , C , and D (with their respective errors) were employed to extract the contribution of each process to the overall integral of the experimental distribution generated by the $^{17}\text{O} + ^{58}\text{Ni}$ interaction. These contributions were fitted by second order polynomials as a function of the angle in the center of mass frame, as shown in Fig. 4. The contribution arising from the projectile excitation was found to be negligible at all angles covered by detector C and at all energies. The procedure discussed above was

repeated at each energy, and its results have been employed in a further pixel-by-pixel integration of the peaks, corresponding to the $^{17}\text{O} + ^{58}\text{Ni}$ collision, recorded by the backward detector. Besides the errors resulting from the fit of Eq. (3.1), an additional error in the discrimination of the different processes is related to the simulated FWHM of the peak for processes **a**, **b**, **c**, and **d**, since a 200 keV change (the maximum one allowed from the study of the $^{17}\text{O} + ^{208}\text{Pb}$ elastic scattering spectra) in the distribution FWHM would result in a 0.03 maximum error in the fraction determination. Errors bars in Fig. 4 include both uncertainties.

B. Pixel-by-pixel analysis

The integration of the events was performed pixel by pixel, correlating the energy deposition in the horizontal (front) strips with that in the vertical (back) strips. Figure 5 shows a typical pixel correlation plot for horizontal strip number 8 versus vertical strip number 8 of detector A at $E_{\text{lab}} = 50$ MeV. Full energy peaks were integrated by applying elliptical contours around the two spots indicated by the arrows. Events not belonging to the full energy peaks (i.e., interstrip in either detector side or background events) were rejected [29].

The distribution of integrals for ^{17}O particles scattered from the ^{208}Pb backing was used to cross-check the apparatus geometry, exploiting the symmetries with respect to both the beam axis and the Y axis of each DSSSD. The accuracy of the detector array geometry, deduced by means of the described procedure, was of the order of ~ 0.2 mm in the vertical position of the telescopes and $\sim 0.5^\circ$ in their angular placement.

The contributions of each process were obtained by multiplying the total number of counts extracted from the spots corresponding to the $^{17}\text{O} + ^{58}\text{Ni}$ collisions by the coefficients A , B , C , and D resulting from the second-order parametrization defined in the previous subsection (see Sec. III A and Fig. 4).

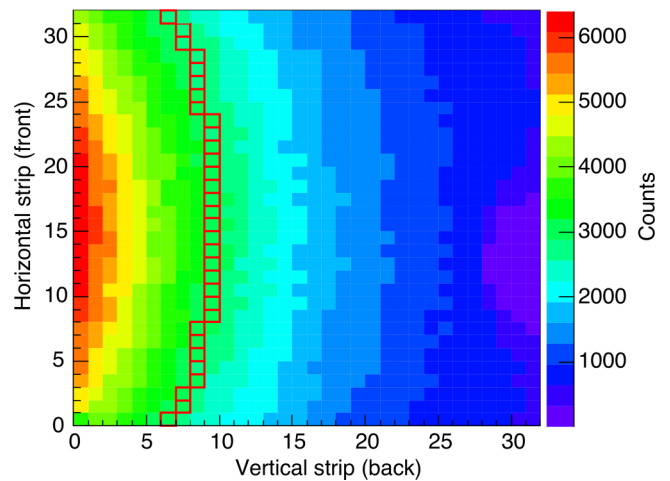


FIG. 6. Distribution of ^{17}O particles elastically scattered from the ^{208}Pb target at $E_{\text{lab}} = 50$ MeV and detected by detector A. Pixels corresponding to $\theta_{\text{c.m.}} \simeq 55^\circ$ were grouped together and highlighted.

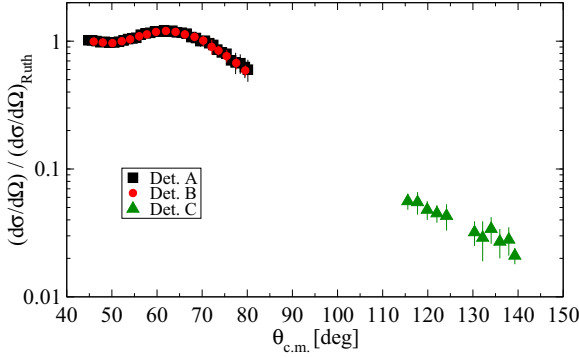


FIG. 7. Elastic scattering angular distributions for $^{17}\text{O} + ^{58}\text{Ni}$ at $E_{\text{lab}} = 50$ MeV. In the forward angular range, data from detector A (black squares) flawlessly overlap with those from detector B (red circles). Data from detector C, at backward angles, are plotted as green triangles.

C. Elastic scattering

In the explored energy range, the elastic scattering of ^{17}O from ^{208}Pb is purely of Rutherford type and can be used for the normalization of the scattering data collected for the $^{17}\text{O} + ^{58}\text{Ni}$ system. Since the two scattering processes were measured simultaneously, the incident flux is identical for both collisions and, according to the definition of cross section, the ratio to Rutherford cross section in the center-of-mass frame for the $^{17}\text{O} + ^{58}\text{Ni}$ system was extracted as follows:

$$\left(\frac{d\sigma}{d\sigma_{\text{R}}}\right)_{\text{c.m.}}^{\text{Ni}} = \frac{N_{\text{c}}^{\text{Ni}} J^{\text{Ni}} \xi^{\text{Pb}}}{N_{\text{c}}^{\text{Pb}} J^{\text{Pb}} \xi^{\text{Ni}}} \frac{d\sigma_{\text{R}}^{\text{Pb}}}{d\sigma_{\text{R}}^{\text{Ni}}}, \quad (3.2)$$

where N_{c}^{Ni} and N_{c}^{Pb} were obtained by means of the process discrimination procedure described in Sec. III A and the integration procedure described in Sec. III B and denote the number of detected ^{17}O particles elastically scattered from the ^{58}Ni target and the ^{208}Pb backing, respectively; J^{Ni} (J^{Pb}) is the Jacobian of the coordinate transformation from the laboratory to center of mass frame; ξ^{Ni} (ξ^{Pb}) is the thickness of the ^{58}Ni target (^{208}Pb backing); and $d\sigma_{\text{R}}^{\text{Ni}}$ ($d\sigma_{\text{R}}^{\text{Pb}}$) is the Rutherford differential cross section in the center-of-mass frame ($d\sigma/d\Omega$) for the scattering of ^{17}O particles from the ^{58}Ni target (^{208}Pb backing). Equation (3.2) allows us to extract the ratio to Rutherford cross section, for each pixel in detectors A, B, and C, without any further normalization constant. The results of this procedure were grouped by pixels belonging to the same polar angle $\theta_{\text{c.m.}}$, as shown in Fig. 6, within an interval of 1° for detector A and 2° for detectors B and C. For each group of pixels the average cross section and its statistical error were evaluated. A 2% error was added to take into account the uncertainty in the ratio between the thicknesses of the Pb and Ni layers. The uncertainty related to the process discrimination procedure (see Sec. III A) was also added in quadrature.

The elastic scattering angular distribution extracted using this procedure for $E_{\text{lab}} = 50$ MeV is shown in Fig. 7. The angular distributions, at forward angles, show that the data from detector B flawlessly overlap with those provided by detector A which has a higher granularity (i.e., better angular

resolution). Therefore, in the following steps of the analysis only the data provided by detector A were considered.

The extracted $^{17}\text{O} + ^{58}\text{Ni}$ elastic scattering angular distributions were analyzed within the framework of the optical model as will be described in Sec. IV.

D. ^{58}Ni target inelastic excitation

Following the procedure described in the previous subsection, it was possible to extract the angular distribution for the inelastic excitation of the target. The number of detected ^{17}O particles which were scattered by the ^{58}Ni target leaving it in its first excited state ($N_{\text{ex}}^{\text{Ni}}$) was extracted by multiplying the total peak integral by the contribution from this process. In this case Eq. (3.2) had to be adjusted in order to extract the angular distribution in units of mb/sr:

$$\left(\frac{d\sigma_{\text{ex}}}{d\Omega}\right)_{\text{c.m.}}^{\text{Ni}} = \frac{N_{\text{ex}}^{\text{Ni}} J^{\text{Ni}} \xi^{\text{Pb}}}{N_{\text{c}}^{\text{Pb}} J^{\text{Pb}} \xi^{\text{Ni}}} \left(\frac{d\sigma_{\text{R}}}{d\Omega}\right)_{\text{c.m.}}^{\text{Pb}} \quad (3.3)$$

with the same notation as Eq. (3.2).

As before, the average cross section and its statistical error were calculated for each group of pixels. The error due to the uncertainty in the target thickness and the statistical error due to the process discrimination procedure were added to the statistical error on the average cross section. In Fig. 8 the extracted angular distributions for target excitation are compared with coupled channel (CC) predictions calculated with the experimental $B(E2)$ transition probability [30] and a nuclear deformation length $\delta_2 = 1.2$ fm obtained from CC fit to the $^{16}\text{O} + ^{58}\text{Ni}$ inelastic scattering data of Ref. [31] using the code FRESKO [32]. At this stage of the analysis the elastic scattering angular distributions were fitted using FRESKO in order to calculate the theoretical curves for the target excitation, which compare well with the extracted angular distributions. At $E_{\text{lab}} = 40$ MeV the contribution of the target inelastic excitation to the peak corresponding to the $^{17}\text{O} + ^{58}\text{Ni}$ interaction was less than 1%, definitely too small to be correctly extracted by the discrimination technique (see Sec. III A). Therefore, since the data for all other energies were well reproduced, the contribution due to target excitation at $E_{\text{lab}} = 40$ MeV was kept as a fixed parameter in the discrimination procedure.

E. One-neutron stripping

Following the same procedure as in the previous two subsections it was also possible to obtain angular distributions for the $1n$ stripping process. The number of detected ^{16}O particles ($N_{\text{tr}}^{\text{Ni}}$) was extracted by multiplying the overall peak integral by the contribution corresponding to this process. In this case, the angular distribution in units of mb/sr is given by the formula

$$\left(\frac{d\sigma_{\text{tr}}}{d\Omega}\right)_{\text{c.m.}}^{\text{Ni}} = \frac{N_{\text{tr}}^{\text{Ni}} J^{\text{Ni}} \xi^{\text{Pb}}}{N_{\text{c}}^{\text{Pb}} J^{\text{Pb}} \xi^{\text{Ni}}} \left(\frac{d\sigma_{\text{R}}}{d\Omega}\right)_{\text{c.m.}}^{\text{Pb}} \quad (3.4)$$

with the same notation as Eq. (3.2).

As before, the average cross section and its error were computed for each group of pixels. The extracted angular distributions for the one-neutron stripping process are plotted

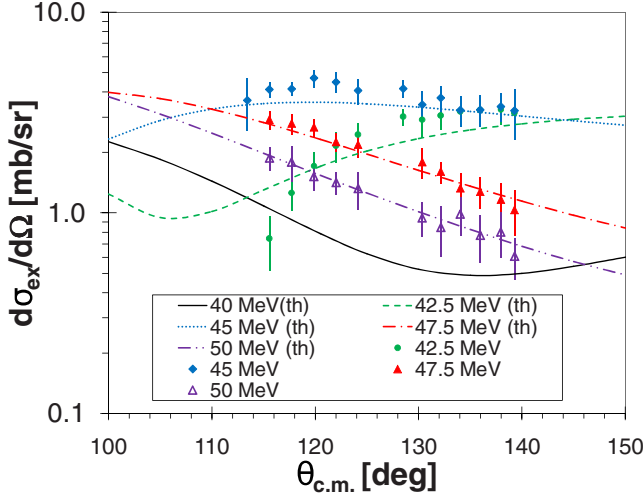


FIG. 8. Angular distributions for target excitation to its first excited state ($E^* = 1.454$ MeV, $J^\pi = 2^+$). These angular distributions are compared with CC calculations for the four highest beam energies: 42.5 MeV (green circles), 45 MeV (blue diamonds), 47.5 MeV (red triangles), and 50 MeV (hollow purple triangles). At $E_{\text{lab}} = 40$ MeV, the contribution to the integrated peak was not discriminated; see text for details.

in Fig. 9. Coupled-channel Born-approximation (CCBA) calculations were performed with FRESKO to model this reaction. The entrance partition included inelastic coupling to the 0.87 MeV $1/2^+$ excited state of ^{17}O with the $B(E2)$ value taken from Ref. [33] and the nuclear deformation length $\delta_2 = 1.2$ fm obtained from a fit to the $^{17}\text{O} + ^{60}\text{Ni}$ inelastic scattering data of Ref. [34]. In the exit channel inelastic coupling to the 6.13 MeV 3^- excited state of ^{16}O was included with the $B(E3)$ value taken from Ref. [35] and the nuclear deformation length $\delta_3 = 1.71$ fm obtained from a fit to the proton inelastic

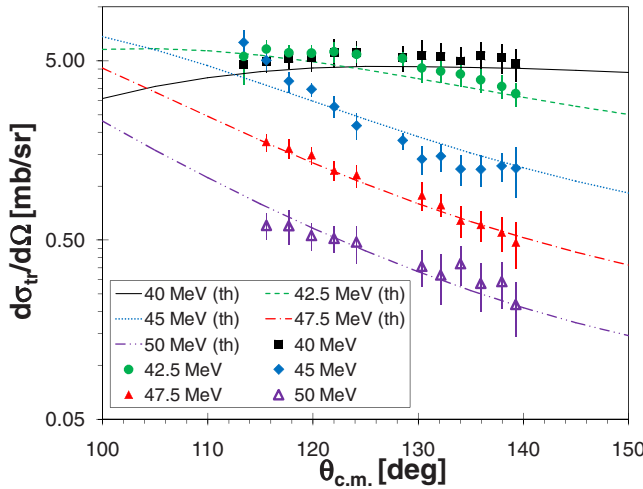


FIG. 9. Angular distributions for the $1n$ stripping process at five beam energies: 40 MeV (black squares), 42.5 MeV (green circles), 45 MeV (blue diamonds), 47.5 MeV (red triangles), and 50 MeV (hollow purple triangles). These angular distributions are compared with CCBA calculations; see text for details.

TABLE I. States in ^{59}Ni and spectroscopic amplitudes from Ref. [38] employed in the CCBA calculations for the $1n$ -stripping process.

E^* (MeV)	J^π	C^2S	E^* (MeV)	J^π	C^2S
0.00	$3/2^-$	0.537	3.06	$9/2^+$	0.381
0.34	$5/2^-$	0.687	4.51	$5/2^+$	0.154
0.47	$1/2^-$	0.538	5.16	$1/2^+$	0.124
0.88	$3/2^-$	0.073	5.54	$1/2^+$	0.109
1.30	$1/2^-$	0.339	5.69	$1/2^+$	0.127
1.68	$5/2^-$	0.104			

scattering data of Ref. [36]. Spectroscopic amplitudes for the $(^{17}\text{O}(5/2^+_1) | ^{16}\text{O}(0^+_1) + n)$, $(^{17}\text{O}(1/2^+_1) | ^{16}\text{O}(0^+_1) + n)$, and $(^{17}\text{O}(5/2^+_1) | ^{16}\text{O}(3^-_1) + n)$ overlaps were taken from Ref. [37]. Spectroscopic amplitudes for the $(^{59}\text{Ni} | ^{58}\text{Ni} + n)$ overlaps were taken from Ref. [38] for the states in ^{59}Ni and are listed in Table I. The entrance channel optical potentials were obtained from CC fits to the appropriate $^{17}\text{O} + ^{58}\text{Ni}$ elastic scattering data and the exit channel potentials were obtained from CC fits to the 44 MeV $^{16}\text{O} + ^{58}\text{Ni}$ elastic scattering data of Ref. [39]. The calculated $1n$ -stripping angular distributions were found to be not very sensitive to the choice of the exit channel potential. The experimental angular distributions are well described by the theoretical curves and their integration with respect to angle allows the evaluation of an overall cross section for the $1n$ stripping process.

IV. OPTICAL MODEL ANALYSIS

A. First approach (WS-WS)

An optical model analysis of the elastic scattering data was performed using the code FRESKO. The first approach employed the Woods-Saxon (WS) potentials for both parts of the OMP:

$$V(r) = -\frac{V_0}{e^{\frac{r-R}{a^R}} + 1}, \quad W(r) = -\frac{W_0}{e^{\frac{r-R'}{a^{I'}}} + 1}, \quad (4.1)$$

where V_0 (W_0) [MeV] is the potential depth of the real (imaginary) part, a^R ($a^{I'}$) [fm] is the diffuseness parameter for the real (imaginary) part, and the radius parameter for the

TABLE II. Best-fit real (V_0) and imaginary (W_0) depths of the OMP obtained by fitting the angular distributions with a Woods-Saxon potential for both real and imaginary parts. The error correlation coefficient ρ is also listed. The geometrical parameters were fixed as follows: $r_0^R = 1.16$ fm, $a^R = 0.70$ fm, $r_0^{I'} = 1.39$ fm, and $a^{I'} = 0.3$ fm.

E_{lab} (MeV)	V_0 (MeV)	W_0 (MeV)	χ^2/N	ρ
40.0	55 ± 3	2.7 ± 0.8	0.400	0.471
42.5	49 ± 2	6.2 ± 2.0	0.201	0.580
45.0	49 ± 2	11 ± 2	0.405	0.912
47.5	48 ± 1	11 ± 1	0.217	0.844
50.0	47 ± 1	14 ± 1	0.605	0.821

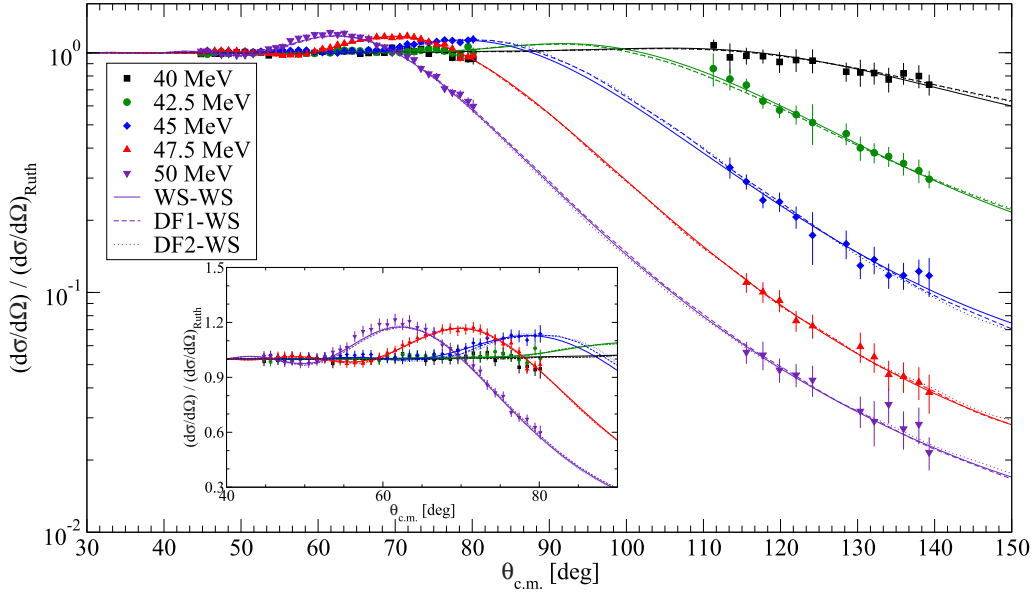


FIG. 10. Elastic scattering angular distributions for $^{17}\text{O}+^{58}\text{Ni}$ at five energies in the explored range. At forward angles the angular distributions extracted from detector A are plotted, whereas at backward angles the plotted angular distributions are extracted from detector C. Solid lines (WS-W) correspond to fits using the first approach (Woods-Saxon potentials for both real and imaginary parts). Dashed lines (DF1-W) correspond to the fits for the second approach (double folding potential for the real part and a Woods-Saxon potential for the imaginary part). Dotted lines (DF2-W) correspond to the fits for the third approach (double folding potential with different densities for the real part and a Woods-Saxon potential for the imaginary part). The inset shows a detail of the forward angle range where the Coulomb-nuclear interference pattern is evident.

real (imaginary) part, R^R (R^I) [fm], is given by

$$R^R = r_0^R \left(A_P^{\frac{1}{3}} + A_T^{\frac{1}{3}} \right), \quad R^I = r_0^I \left(A_P^{\frac{1}{3}} + A_T^{\frac{1}{3}} \right), \quad (4.2)$$

where r_0^R (r_0^I) is the reduced radius parameter of the real (imaginary) part of the OMP and A_P (A_T) is the projectile (target) mass number. In the first step of this analysis all six parameters were let free. The resulting geometrical parameters (r_0 and a) were rather similar, especially for the three highest energies (45, 47.5, and 50 MeV), where the deviations of the angular distributions from Rutherford scattering are more pronounced. In the second step, the angular distributions were fitted keeping the geometrical parameters fixed at their average values ($r_0^R = 1.16 \pm 0.13$ fm, $a^R = 0.70 \pm 0.17$ fm for the real part and $r_0^I = 1.39 \pm 0.03$ fm, $a^I = 0.3 \pm 0.1$ fm for the

imaginary part of the OMP) and only the potential depths of the real and imaginary part were let free. The average geometrical parameters are consistent with the literature for systems involving the same projectile (in particular with Ref. [40]) and their uncertainties are the statistical errors of the average values. Table II lists the resulting fit parameters, namely the depths of the real (V_0) and imaginary (W_0) parts of the OMP. The fits are plotted as the solid curves in Fig. 10.

B. Second approach (DF1-W)

As a second approach, the elastic scattering angular distributions were fitted by using the double folding procedure [41] for the real part and a Woods-Saxon potential for the imaginary part of the OMP. The double folding potential was

TABLE III. Best-fit OMP parameters obtained using a double folding potential for the real part and a Woods-Saxon potential for the imaginary part (DF1-W). N_R is the scaling coefficient for the real double folding potential whereas W_0 is the potential depth of the imaginary Woods-Saxon potential. The geometrical parameters were fixed as follows: $r_0^I = 1.44$ fm and $a^I = 0.25$ fm.

E_{lab} (MeV)	N_R	W_0 (MeV)	χ^2/N	ρ
40.0	1.23 ± 0.03	2.9 ± 1.6	0.358	0.450
42.5	1.19 ± 0.02	4.8 ± 0.9	0.271	0.058
45.0	1.12 ± 0.01	4.92 ± 0.01	0.405	0.467
47.5	1.17 ± 0.01	6.3 ± 0.3	0.217	0.511
50.0	1.12 ± 0.02	7.8 ± 0.4	0.605	0.737

TABLE IV. Best-fit OMP parameters obtained using the third approach (DF2-W); see text for details. N_R is the scaling coefficient for the real double folding potential, whereas W_0 is the potential depth of the imaginary Woods-Saxon potential. The geometrical parameters were fixed as follows: $r_0^I = 1.44$ fm and $a^I = 0.24$ fm.

E_{lab} (MeV)	N_R	W_0 (MeV)	χ^2/N	ρ
40.0	1.24 ± 0.04	2.9 ± 1.5	0.408	0.438
42.5	1.20 ± 0.03	5.0 ± 0.9	0.237	0.284
45.0	1.11 ± 0.01	4.5 ± 0.3	0.429	0.021
47.5	1.18 ± 0.02	6.1 ± 0.3	0.217	0.545
50.0	1.18 ± 0.02	7.8 ± 0.3	0.657	0.589

evaluated as follows:

$$V_{df}(\vec{r}) = \iint \rho_1(\vec{r}_1)\rho_2(\vec{r}_2)V_{nn}(\vec{r}, \vec{r}_1, \vec{r}_2)d\vec{r}_1d\vec{r}_2, \quad (4.3)$$

where ρ_1 and ρ_2 are the projectile [42] and target [43] nuclear matter densities, respectively, and V_{nn} is the M3Y nucleon-nucleon effective interaction [41]. The double folding potential was calculated with the code DFPOT [44]. The charge density of Ref. [43] was converted to a matter density following the procedure of Ref. [45]. In this case the only free parameter for the real part of the OMP was the scaling coefficient N_R . As a first step the angular distributions were fitted, for all energies, leaving the normalization coefficient of the double folded real part and all three parameters of the Woods-Saxon imaginary part free. As in the previous approach, the average values of the geometrical parameters were calculated ($r_0^I = 1.44 \pm 0.03$ fm and $a^I = 0.25 \pm 0.04$ fm) for the imaginary part and then kept fixed for a further fit of the elastic scattering angular distributions. The parameters resulting from this fit, namely the scaling coefficient for the real part (N_R) and the depth of the imaginary part (W_0) of the OMP, are listed in Table III. The angular distributions corresponding to this approach are plotted in Fig. 10 as the dashed lines.

C. Third approach (DF2-WS)

The third approach was similar to the second but this time the projectile and target densities were taken from the RIPL-3 web-site [46] and were calculated using the Hartree-Fock-Bogolubov (HFB) method based on the BSk14 Skyrme force [47]. As in the other two approaches the angular distributions were initially fitted, at all energies, leaving free the normalization coefficient of the double folding real part and the three parameters of the Woods-Saxon imaginary part. The fitting procedure was then repeated fixing the geometrical parameters of the imaginary part of the OMP at the average values, namely $r_0^I = 1.44 \pm 0.03$ fm and $a^I = 0.24 \pm 0.03$ fm. The resulting parameters, the scaling coefficient of the real part (N_R) and the potential depth of the imaginary part (W_0), are listed in Table IV. The fits corresponding to the third approach are plotted in Fig. 10 as the dotted lines.

D. Total reaction cross section

The total reaction cross section may also be obtained from the best fits to the elastic scattering angular distributions. The extracted total reaction cross sections for the three approaches and their weighted averages (with the errors of the weighted average) are reported, for all energies, in Table V. The energies in the center of mass system were corrected by taking into account the energy losses (~ 300 keV) in half of the ^{58}Ni target thickness.

V. DISCUSSION

The results of the three OMP analyses are compared with each other in Fig. 10 and clearly show good agreement between the fits corresponding to the three different approaches. The trends of the depths of the real and imaginary parts of the OMP as a function of the incident energy are plotted in Fig. 11.

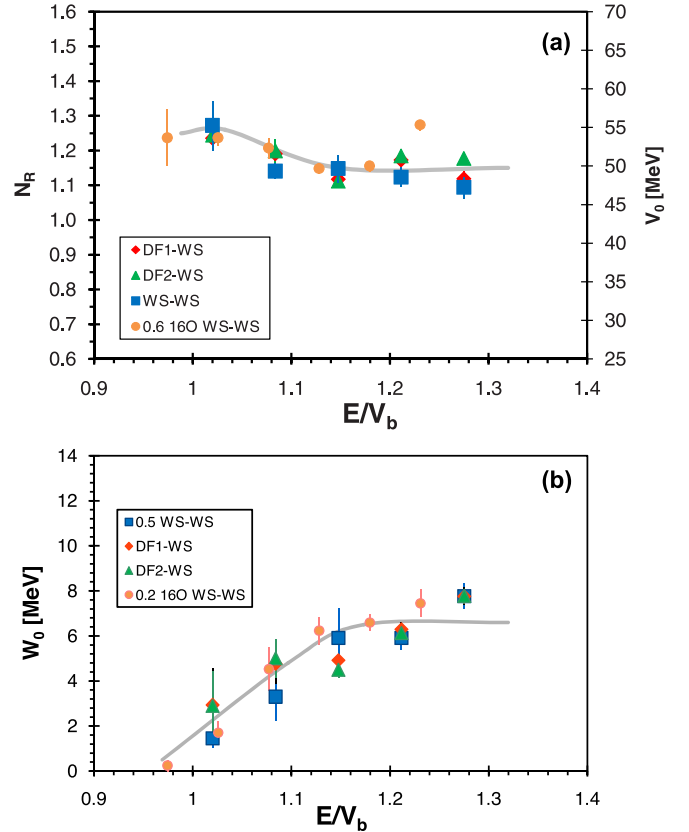


FIG. 11. Trends of (a) the real part and (b) the imaginary part of the OMP as a function of the ratio to the Coulomb barrier of the incident energy ($V_b^{c.m.} = 30.32$ MeV, $V_b^{lab} = 39.21$ MeV). Blue squares, red diamonds, and green triangles represent the first (WS-WS), second (DF1-WS), and third (DF2-WS) analyses, respectively; see text for additional details. Orange circles represent the scaled results for the $^{16}\text{O} + ^{58}\text{Ni}$ system from Ref. [39]. The solid line is intended to guide the eye.

In this figure the depths of the WS-WS best-fit potentials were directly compared with the other two approaches. Both the real and imaginary parts show similar behavior for all three approaches: as the incident energy decreases, the usual reduction of the imaginary part and a hint of a “bump” in the real part is observed, although the lowest energy point lies slightly above the Coulomb barrier. The behavior of both real and imaginary parts of the OMP is similar to that found for the $^{16}\text{O} + ^{58}\text{Ni}$ system in Ref. [39,49] and is consistent with the classic “threshold anomaly” [16,52], contrary to what was observed, for instance, for the pair ^6Li ($S_d = 1.47$ MeV) and ^7Li on various targets ([21] and references therein). Deviations from the standard threshold anomaly behavior seem to be related to the projectile binding energy and this may imply a connection with the breakup process [22]. Furthermore the similar results obtained for the DF1-WS and the DF2-WS approaches suggest that the study of the TA is not influenced by the density distribution used for ^{17}O .

Table V reports the total reaction cross sections for the three approaches. The weighted averages, listed in the second to last column, were employed for a comparison with the total

TABLE V. Total reaction cross sections extracted from the three optical model analyses as a function of the collision energy in the center-of-mass frame, $E_{c.m.}$: Woods-Saxon potential for both real and imaginary parts (σ_{WS}), double folding potential DF1 for the real part and Woods-Saxon potential for the imaginary part (σ_{DF1}), double folding potential DF2 for the real part, and Woods-Saxon potential for the imaginary part (σ_{DF2}). Results with all parameters free (“free”) and with fixed geometry (“fixed”) are reported. The weighted average $\langle\sigma\rangle$ and the $1n$ -stripping cross section (σ_{tr} extracted by integrating the CCBA curves) are also indicated.

$E_{c.m.}$ (MeV)	σ_{WS} (mb)		σ_{DF1} (mb)		σ_{DF2} (mb)		$\langle\sigma\rangle$ (mb)	σ_{tr} (mb)
	free	fixed	free	fixed	free	fixed		
30.7	47	40	46	44	46	45	45 ± 14	28
32.6	198	156	160	170	159	170	170 ± 12	36
34.6	277	314	321	309	321	306	313 ± 12	41
36.5	449	448	456	459	457	457	456 ± 6	44
38.5	549	580	584	584	585	587	573 ± 9	45

reaction cross sections extracted for the $^{17}\text{F} + ^{58}\text{Ni}$ system [48], ^{17}F being the mirror nucleus of ^{17}O , and for the $^{16}\text{O} + ^{58}\text{Ni}$ system [49,50]. To make comparable different systems, the energies in the center of mass reference frame and the reaction cross sections were scaled according to the procedure described in Ref. [51]. As may be seen in Fig. 12, the total reaction cross section for the $^{17}\text{O} + ^{58}\text{Ni}$ system is essentially the same as $^{16}\text{O} + ^{58}\text{Ni}$ system at the higher energies but definitely becomes larger as the energy is decreased towards the Coulomb barrier. Concerning the comparison between total reaction cross sections of $^{17}\text{F} + ^{58}\text{Ni}$ and $^{17}\text{O} + ^{58}\text{Ni}$ systems, nothing conclusive can be said due to the large uncertainties in the available data, although there is some evidence for greater absorption at the lower of the two energies. The $^{17}\text{F} + ^{58}\text{Ni}$ system hence deserves further investigation, since more energy points are necessary, with better accuracy if possible.

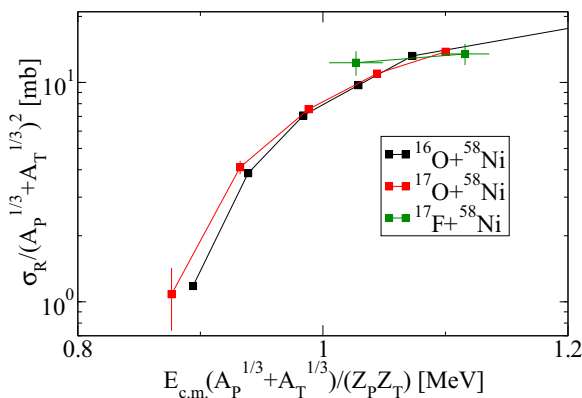


FIG. 12. Total reaction cross sections for the $^{17}\text{O} + ^{58}\text{Ni}$, $^{17}\text{F} + ^{58}\text{Ni}$ [48], and $^{16}\text{O} + ^{58}\text{Ni}$ [39,49,50] systems compared. The energy in the center of mass system was scaled to the Coulomb barrier, whereas the reaction cross sections were scaled to the system mass according to the procedure described in Ref. [51]. Where not visible, error bars are beneath the symbol.

VI. CONCLUSIONS

In this work a new high-granularity experimental setup was employed to investigate several direct processes occurring in the $^{17}\text{O} + ^{58}\text{Ni}$ collision at five beam energies around the Coulomb barrier. We dealt with the experimental difficulties in the discrimination of different reaction channels leading to very similar conditions in the exit channel. The contributions of overlapping phenomena were disentangled by means of a technique based on Monte Carlo simulations. The necessary conditions for the success of this method are several: the processes contributing to the same peak must generate noticeable structures; they should contribute at least 1% of the total peak integral; and the detector energy calibration should be accurate. Due to these constraints the discrimination of processes, employed here for the $^{17}\text{O} + ^{58}\text{Ni}$ collision at backward angles only and over a limited energy range, cannot be considered a universal method despite the good results achieved for the studied collision. However, it could be a useful technique for radioactive beam experiments under the proper conditions.

The angular distributions for the target excitation to its first excited state was extracted at backward angles using the discrimination technique, and they compared well with CC calculations. The backward angle angular distributions for the one-neutron stripping were similarly well described by CCBA calculations. The good agreement obtained between the calculations and the data for these two processes provides a self-consistency check for the pure elastic scattering angular distributions extracted using the discrimination procedure. The elastic scattering angular distributions for the $^{17}\text{O} + ^{58}\text{Ni}$ collision were fitted in the framework of the optical model using three different approaches: (1) Woods-Saxon potentials for both real and imaginary parts of the OMP, (2) a double folding potential for the real part and a Woods-Saxon potential for the imaginary part, and (3) a double folding potential calculated using different densities for the real part and a Woods-Saxon potential for the imaginary part. The variation of the depths of the real and imaginary parts of the OMP as a function of incident energy was similar to that found for the $^{16}\text{O} + ^{58}\text{Ni}$ system [39,49], displaying a conventional, if somewhat weak, threshold anomaly.

A comparison of the total reaction cross sections for the $^{16,17}\text{O}$, $^{17}\text{F} + ^{58}\text{Ni}$ systems showed that above the Coulomb barrier the ^{16}O and $^{17}\text{O} + ^{58}\text{Ni}$ σ_R are identical. Unfortunately the large uncertainties on the available $^{17}\text{F} + ^{58}\text{Ni}$ σ_R do not permit any definitive conclusions to be drawn, although there is some evidence for larger absorption in this system as the incident energy approaches the Coulomb barrier, presumably due to the increased relative importance of $^{17}\text{F} \rightarrow ^{16}\text{O} + p$ breakup in this system at lower energies. However, it is clear that the $^{17}\text{O} + ^{58}\text{Ni}$ σ_R becomes larger than that for the $^{16}\text{O} + ^{58}\text{Ni}$ system as the incident energy is decreased towards the Coulomb barrier. This outcome confirms the general conclusion that, at bombarding energies below/around the Coulomb barrier, the reaction cross section for “moderately bound” nuclei results to be systematically higher than those for collisions involving tightly bound ones. In this case, the relatively larger absorption could be due to the increasing importance of the $1n$ -stripping channel for ^{17}O , a suggestion borne out by the calculated cross sections for this process

given in Table V; the $1n$ stripping cross section forms $\sim 60\%$ of the total reaction cross section at 40 MeV, a proportion that declines rapidly as the incident energy is increased.

ACKNOWLEDGMENTS

This work was supported by the Italian Ministero dell'Istruzione dell'Università e della Ricerca within the

project RBFR08P1W2_001 (FIRB 2008), by the University of Padua, Italy, within the project CPDA145301 (PRAT 2014), by the National Science Centre of Poland under Contract No. UMO-2014/14/M/ST2/00738 (COPIN-INFN Collaboration), and by the European Research Council, 7th Framework Program (FP7/2007-2013) under Grant Agreement No. 600376. J.A.L. acknowledges a Marie Curie-Piscopia fellowship at the University of Padova.

-
- [1] L. Canto, P. Gomes, R. Donangelo, and M. Hussein, *Phys. Rep.* **424**, 1 (2006).
- [2] L. Canto, P. Gomes, R. Donangelo, J. Lubian, and M. Hussein, *Phys. Rep.* **596**, 1 (2015).
- [3] J. F. Liang and C. Signorini, *Int. J. Mod. Phys. E* **14**, 1121 (2005).
- [4] N. Keeley, R. Raabe, N. Alamanos, and J. Sida, *Prog. Part. Nucl. Phys.* **59**, 579 (2007).
- [5] H. Zhang, W. Shen, Z. Ren, Y. Ma, W. Jiang, *et al.*, *Nucl. Phys. A* **707**, 303 (2002).
- [6] E. F. Aguilera, J. J. Kolata, F. D. Becchetti, P. A. DeYoung, *et al.*, *Phys. Rev. C* **63**, 061603 (2001).
- [7] A. Di Pietro, P. Figuera, F. Amorini, C. Angulo, *et al.*, *Phys. Rev. C* **69**, 044613 (2004).
- [8] J. Takahashi, M. Munhoz, E. M. Szanto, N. Carlin, *et al.*, *Phys. Rev. Lett.* **78**, 30 (1997).
- [9] A. Di Pietro, V. Scuderi, *et al.*, *Phys. Rev. C* **85**, 054607 (2012).
- [10] A. Di Pietro, G. Randisi, V. Scuderi, L. Acosta, F. Amorini, *et al.*, *Phys. Rev. Lett.* **105**, 022701 (2010).
- [11] E. F. Aguilera, E. Martínez-Quiroz, D. Lizcano, A. Gómez-Camacho, *et al.*, *Phys. Rev. C* **79**, 021601 (2009).
- [12] D. Baye, P. Descouvemont, and M. Hesse, *Phys. Rev. C* **58**, 545 (1998).
- [13] R. Morlock, R. Kunz, A. Mayer, M. Jaeger, A. Müller, *et al.*, *Phys. Rev. Lett.* **79**, 3837 (1997).
- [14] M. Milin, V. Ostashko, Miljani, H. Bohlen, *et al.*, *Eur. Phys. J. A* **41**, 335 (2009).
- [15] M. Dufour and P. Descouvemont, *Phys. Rev. C* **72**, 015801 (2005).
- [16] M. A. Nagarajan, C. C. Mahaux, and G. R. Satchler, *Phys. Rev. Lett.* **54**, 1136 (1985).
- [17] G. Satchler, *Phys. Rep.* **199**, 147 (1991).
- [18] M. Brandan and G. Satchler, *Phys. Rep.* **285**, 143 (1997).
- [19] N. Keeley, S. Bennett, N. Clarke, B. Fulton, G. Tungate, P. Drumm, M. Nagarajan, and J. Lilley, *Nucl. Phys. A* **571**, 326 (1994).
- [20] A. Pakou, N. Alamanos, G. Doukelis, *et al.*, *Phys. Rev. C* **69**, 054602 (2004).
- [21] K. Zerva, A. Pakou, N. Patronis, *et al.*, *Eur. Phys. J. A* **48**, 102 (2012).
- [22] M. S. Hussein, P. R. S. Gomes, J. Lubian, and L. C. Chamon, *Phys. Rev. C* **73**, 044610 (2006); **76**, 019902(E) (2007).
- [23] E. Strano, A. Anastasio, M. Bettini, A. Boiano, C. Boiano, *et al.*, *Nucl. Instrum. Methods Phys. Res., Sect. B* **317**, 657 (2013).
- [24] D. Pierroutsakou *et al.*, *Nucl. Instrum. Methods Phys. Res. Sect. A* **834**, 46 (2016).
- [25] J. F. Ziegler, M. Ziegler, and J. Biersack, *Nucl. Instrum. Methods Phys. Res., Sect. B* **268**, 1818 (2010).
- [26] D. Brink, *Phys. Lett. B* **40**, 37 (1972).
- [27] A. Weber, H. Mommsen, W. Sarter, and A. Weller, *Nucl. Instrum. Methods* **198**, 527 (1982).
- [28] M. Fisichella, A. C. Shotton, A. Di Pietro, *et al.*, *Phys. Rev. C* **92**, 064611 (2015).
- [29] D. Torresi, D. Stanko, A. D. Pietro, *et al.*, *Nucl. Instrum. Methods Phys. Res., Sect. A* **713**, 11 (2013).
- [30] J. M. Allmond, B. A. Brown, A. E. Stuchbery, A. Galindo-Uribarri, *et al.*, *Phys. Rev. C* **90**, 034309 (2014).
- [31] L. West and N. R. Fletcher, *Phys. Rev. C* **15**, 2052 (1977).
- [32] I. J. Thompson, *Comput. Phys. Rep.* **7**, 167 (1988).
- [33] D. M. Manley, B. L. Berman, W. Bertozzi, T. N. Buti, *et al.*, *Phys. Rev. C* **36**, 1700 (1987).
- [34] H. Essel, K. E. Rehm, H. Bohn, H. J. Körner, and H. Spieler, *Phys. Rev. C* **19**, 2224 (1979).
- [35] T. Kibdi and R. Spear, *At. Data Nucl. Data Tables* **80**, 35 (2002).
- [36] S. M. Austin, P. J. Locard, S. N. Bunker, J. M. Cameron, J. R. Richardson, *et al.*, *Phys. Rev. C* **3**, 1514 (1971).
- [37] M. Cavallaro, F. Cappuzzello, M. Bondi, D. Carbone, V. N. Garcia, A. Gargano, *et al.*, *Phys. Rev. C* **88**, 054601 (2013).
- [38] O. Iwamoto, A. Nohtomi, Y. Uozumi, T. Sakae, M. Matoba, M. Nakano, T. Maki, and N. Koori, *Nucl. Phys. A* **576**, 387 (1994).
- [39] L. West, K. W. Kemper, and N. R. Fletcher, *Phys. Rev. C* **11**, 859 (1975).
- [40] G. Goldring, H. Loebenstein, I. Plessner, and M. Sachs, *Phys. Lett. B* **25**, 538 (1967).
- [41] G. Bertsch, J. Borysowicz, H. McManus, and W. Love, *Nucl. Phys. A* **284**, 399 (1977).
- [42] Z. Hu-Yong, S. Wen-Qing, R. Zhong-Zhou, M. Yu-Gang, C. Jin-Gen, *et al.*, *Chin. Phys. Lett.* **20**, 1462 (2003).
- [43] H. D. Vries, C. D. Jager, and C. D. Vries, *At. Data Nucl. Data Tables* **36**, 495 (1987).
- [44] J. Cook, *Comput. Phys. Commun.* **25**, 125 (1982).
- [45] G. Satchler and W. Love, *Phys. Rep.* **55**, 183 (1979).
- [46] R. Capote, M. Herman, P. Obloinsk, P. Young, S. Goriely, T. Belgia, *et al.*, *Nucl. Data Sheets* **110**, 3107 (2009), special issue on nuclear reaction data.
- [47] S. Goriely, M. Samyn, and J. M. Pearson, *Phys. Rev. C* **75**, 064312 (2007).
- [48] M. Mazzocco, C. Signorini, D. Pierroutsakou, T. Glodariu, *et al.*, *Phys. Rev. C* **82**, 054604 (2010).
- [49] N. Keeley, J. Christley, N. Clarke, B. Fulton, *et al.*, *Nucl. Phys. A* **582**, 314 (1995).
- [50] N. Keeley, J. S. Lilley, J. X. Wei, M. Dasgupta, *et al.*, *Nucl. Phys. A* **628**, 1 (1998).
- [51] P. R. S. Gomes, J. Lubian, I. Padron, and R. M. Anjos, *Phys. Rev. C* **71**, 017601 (2005).
- [52] A. Sánchez-Benítez, D. Escrig, M. Álvarez, *et al.*, *Nucl. Phys. A* **803**, 30 (2008).